Atmospheric
Chemistry
and Physics

Supplement of

Observations of the vertical distributions of summertime atmospheric pollutants in Nam Co: OH production and source analysis

Chengzhi Xing et al.

Correspondence to: Cheng Liu (chliu81@ustc.edu.cn) and Chunxiang Ye (c.ye@pku.edu.cn)

Section S1. Vertical retrieval algorithm for MAX-DOAS observation

The atmospheric vertical profile (aerosol, H_2O, NO_2, HONO, and O_3) retrieval algorithm from MAX-DOAS measurements was developed based on the optimal estimation method and used radiative transfer model as the forward model (Lin et al., 2020; Liu et al., 2022; Ji et al., 2023; Xing et al., 2023). The maximum a posteriori state vector x is determined by minimizing the following cost function χ^2.

$$\chi^2 = \left(y - F\left(x,b\right)\right)^T S_\varepsilon^{-1} \left(y - F\left(x,b\right)\right) + \left(x - x_a\right)^T S_a^{-1} \left(x - x_a\right)$$

Here, $F\left(x,b\right)$ is the forward model, which describes the measured DSCDs y as a function of the retrieval state vector x (i.e., aerosol and trace gas vertical profiles) and the meteorological parameters b (e.g., atmospheric pressure and temperature profiles); x_a denotes the a priori vector that serves as an additional constraint; S_ε and S_a are the covariance matrices of y and x_a, respectively. The retrieval of vertical profiles of aerosols and trace gases were classified into two steps. Firstly, we retrieved vertical aerosol profiles based on a series of retrieved O_4 DSCDs at different elevation angles. Secondly, the retrieved aerosol profiles were utilized as the input parameters to the radiative transfer model to retrieve H_2O, NO_2 and HONO profiles. Considering the strong O_3 absorption in the stratosphere, the retrieval of the tropospheric O_3 profile must remove the influence of stratospheric O_3. In this study, daily stratospheric O_3 profiles from TROPOMI measurements were included in the radiative transfer model simulation for tropospheric O_3 profile retrieval to account for the influence of stratospheric O_3 absorption on the retrieval.

Section S2. WRF model configurations

The Weather Research and Forecasting (WRF) model was used to simulate the planetary boundary layer (PBL) height on the Tibetan Plateau. The detailed description of WRF model was given in the WRF website (http://www.wrf-model.org/index.php). In this work, the simulation domain covered 25°N-35°N and 80°E-100°E. The horizontal resolution of this simulation was set to 20×20 km^2, and we set 26 hybrid pressure-sigma levels in the vertical direction. We selected the 6-h final operational global analysis (FNL) data as the initial meteorological fields and boundary conditions. The data were provided by the National Centers for Environmental Prediction (NCEP) with a $1°\times1°$ spatial resolution. Moreover, the NCEP Administrative Data Processing (ADP) Global Surface Observational Weather Data (ds461.0) and Upper Air Observational Weather Data (ds351.0) with 6-h temporal resolution were used to accurately reproduce the methodology. The physical parameterization schemes adopted in this study were described in Table S1.

Table S1. Model physical parameterization schemes.

| Schemes	Description
Microphysics	Purdue Lin Scheme (Chen et al., 2002)
Longwave radiation	Rapid radiative RRTMG Scheme (Iacono et al., 2008)
Shortwave radiation	RRTMG Scheme (Iacono et al., 2008)
Cumulus parameterization	Grell-Freitas Ensemble Scheme (Grell et al., 2014)
Land surface	Unified Noah Land Surface Model (Tewari et al., 2004)
Planetary boundary layer	Yonsei University Scheme (Hong et al., 2006)

33

34
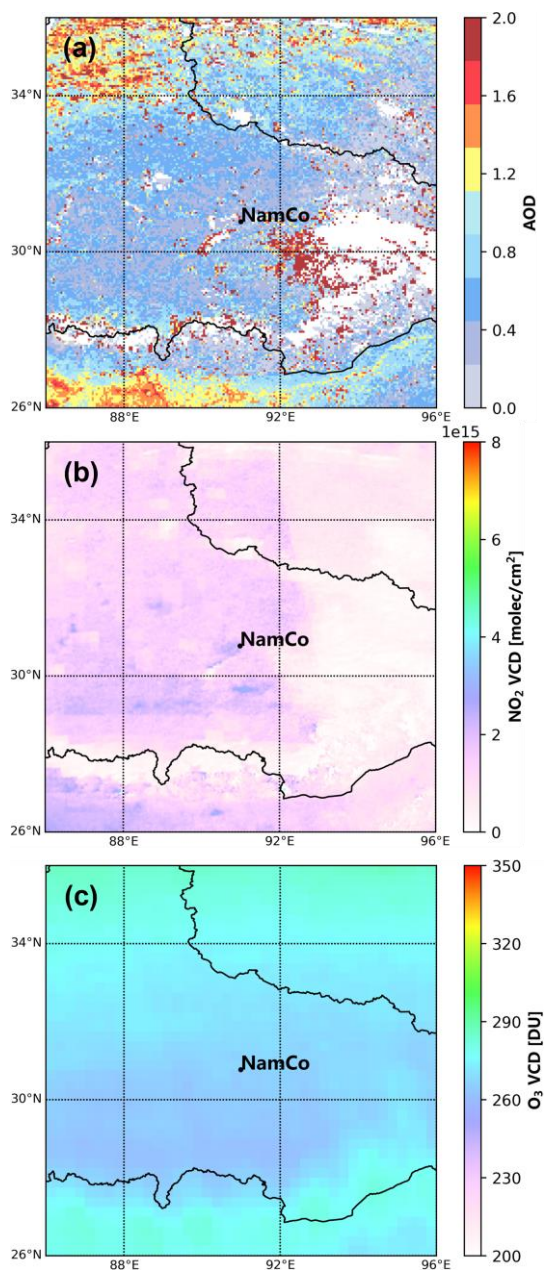
Figure S1. Averaged spatial distributions of (a) AOD monitored by Himawari-8, (b) NO$_2$ VCDs monitored by TROPOMI, (and c) O$_3$ total VCDs monitored by OMI from May to July 2019 in Nam Co.

38

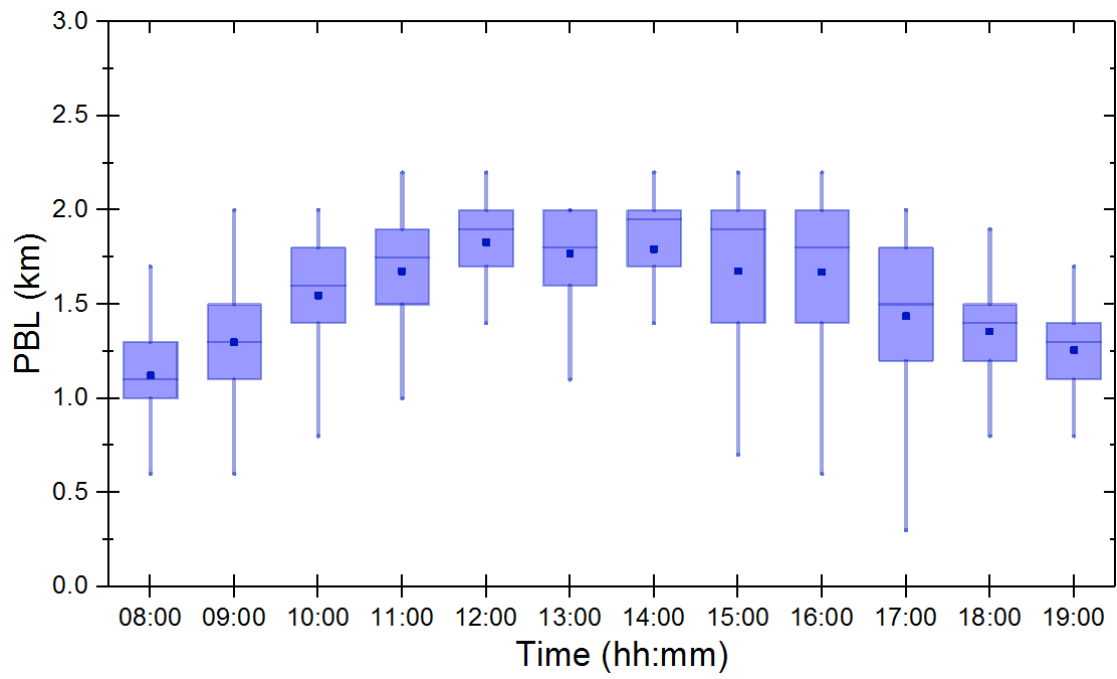39
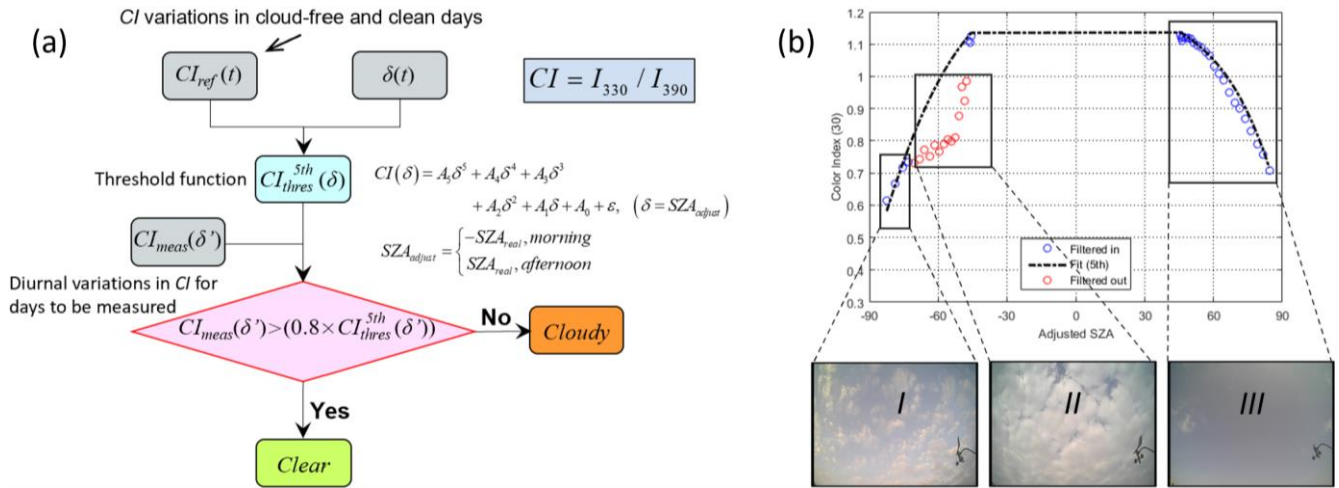
40 Figure S2. (a) Color Index cloud classification algorithm process. (b) Example of cloud classification.

41
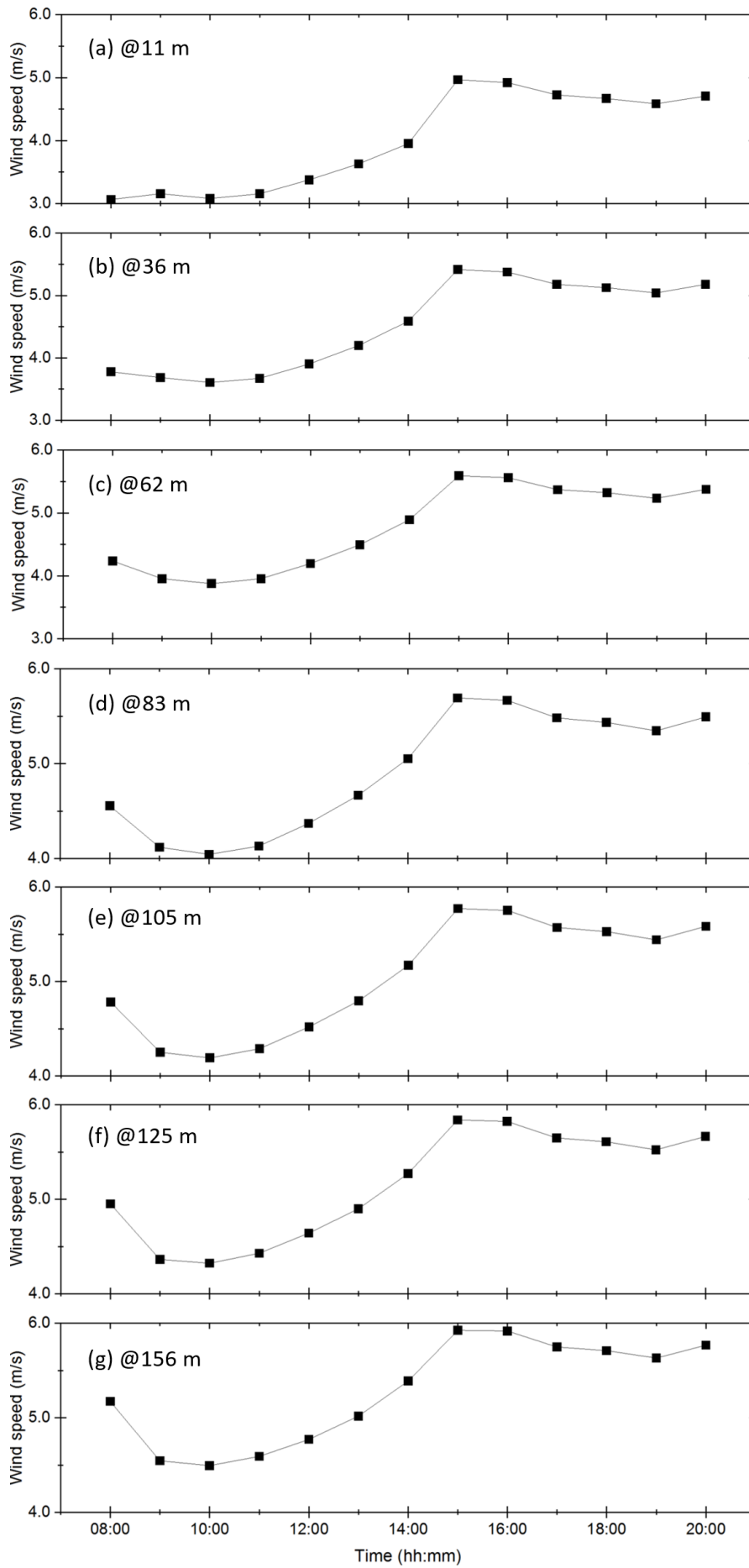
Figure S3. Wind speed at seven different height layers at the measurement site during the measurements.

Figure S4. The diurnal variation of PBL in Nam Co from May to July 2019. The top and bottom of the box represented 75th and 25th percentiles, respectively. The lines and dots within the boxes were the median and mean, respectively.
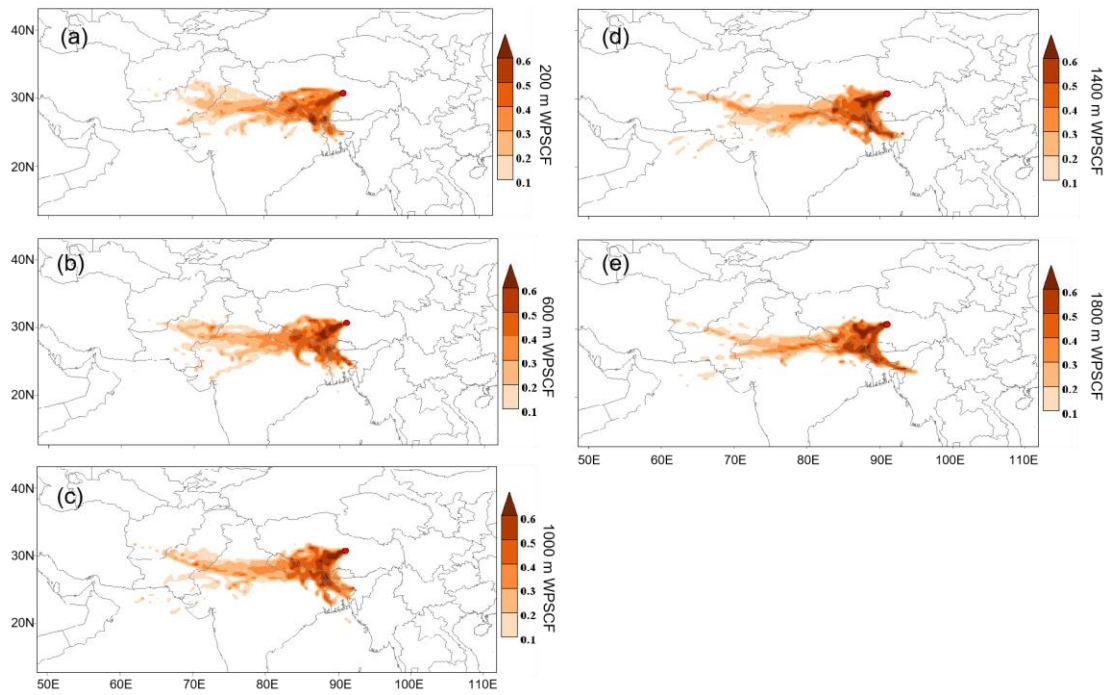
51
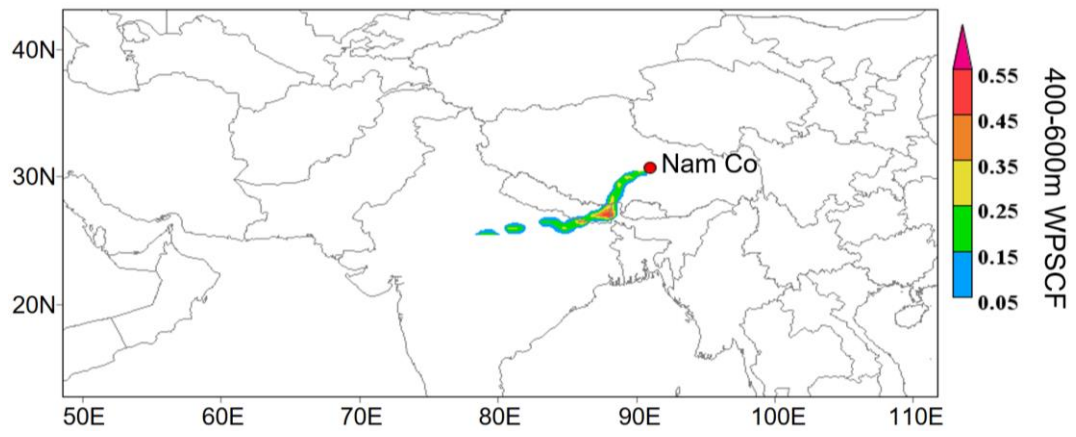
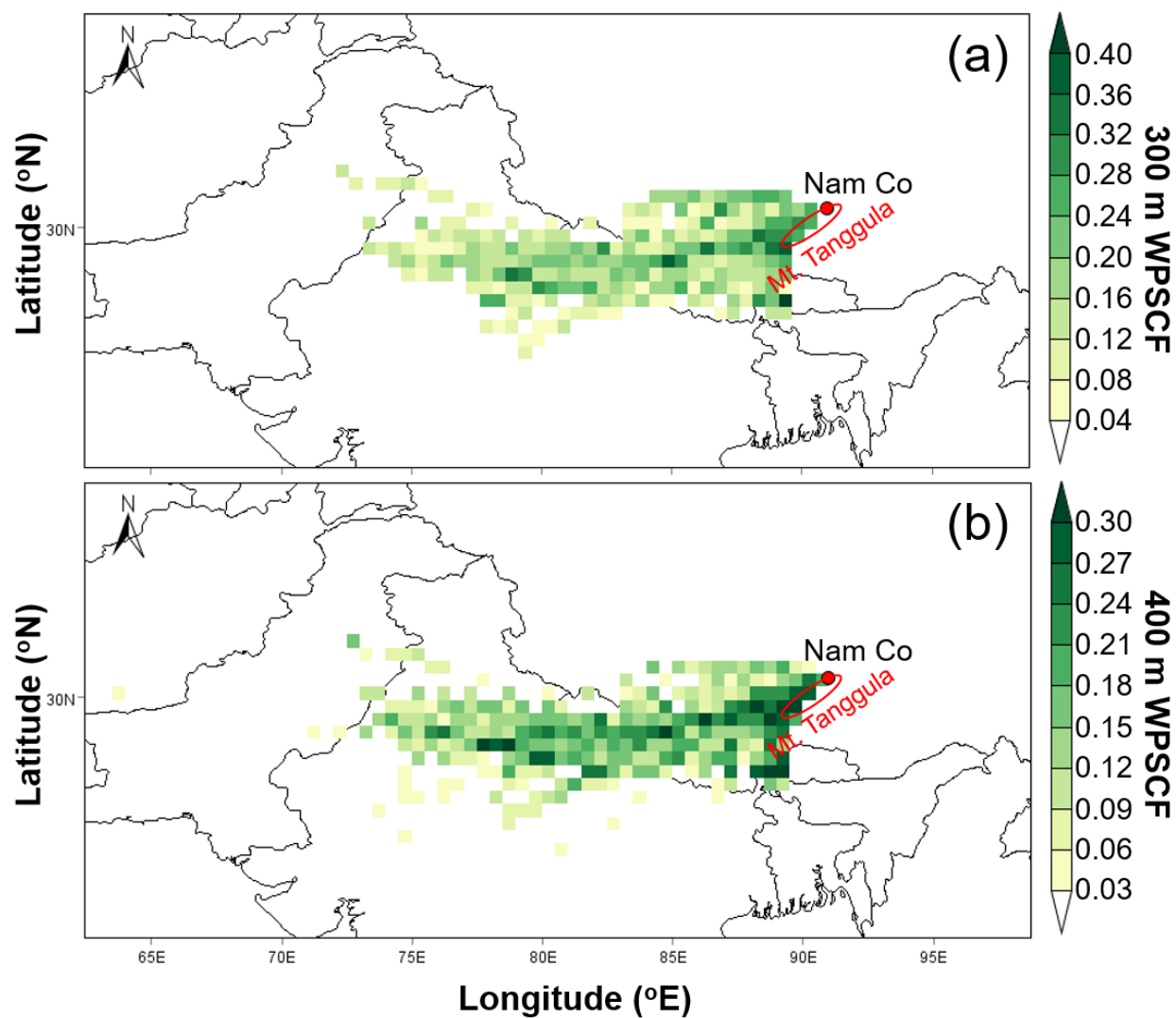52 Figure S5. Spatial distribution of WPSCF values for aerosol at 400-600 m layer on 13th and 30th June.
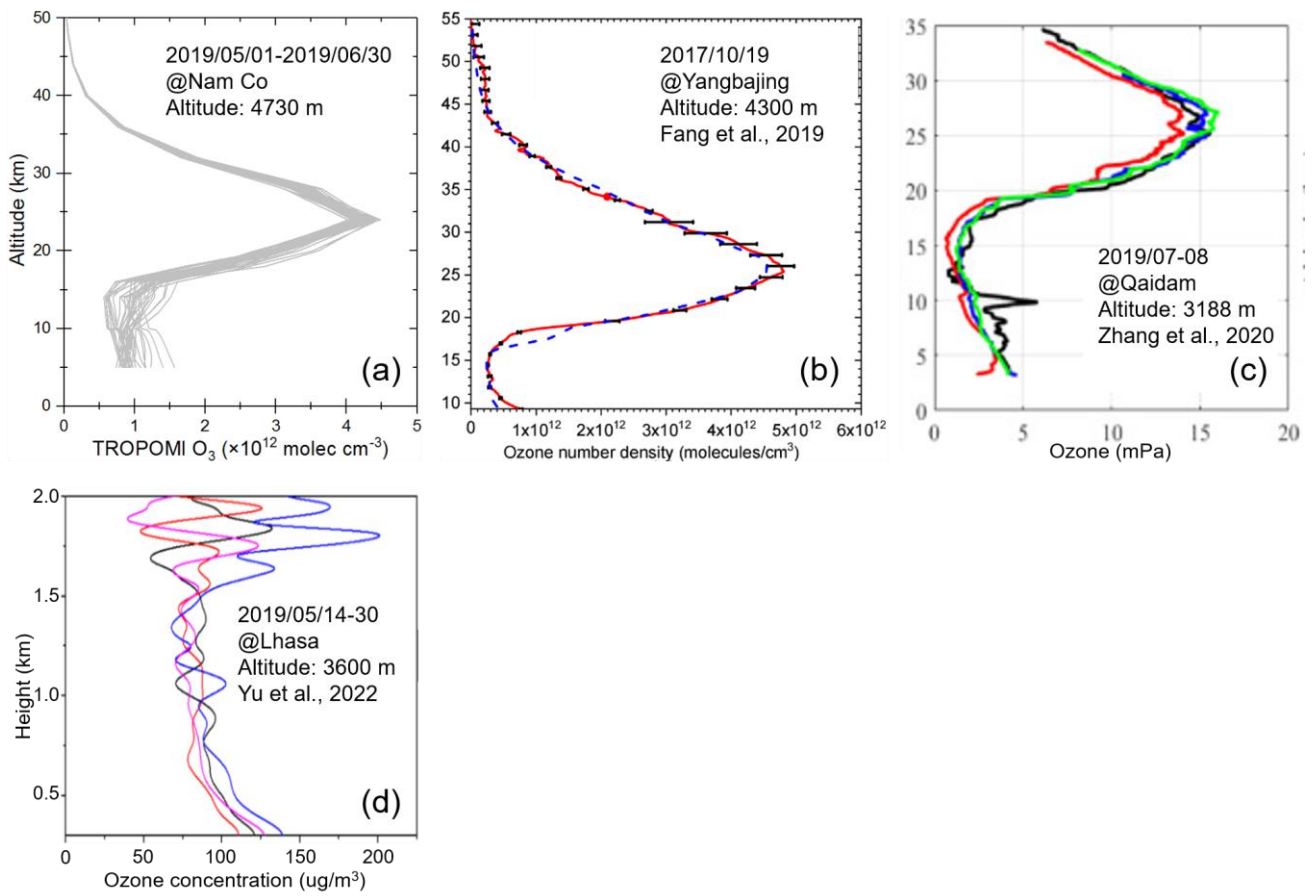
53

54

Figure S6. Spatial distributions of WPSCF values for H_2O at (a) 200 m, (b) 600 m, (c) 1000 m, (d) 1400 m, and (e) 1800 m height layers from 01st May to 09th July 2019 over CAS (NAMORS).

Figure S7. Spatial distributions of 24-h WPSCF values for NO$_2$ at (a) 300 m, and (b) 400 m height layers from 01 May to 09 July 2019 over CAS (NAMORS).
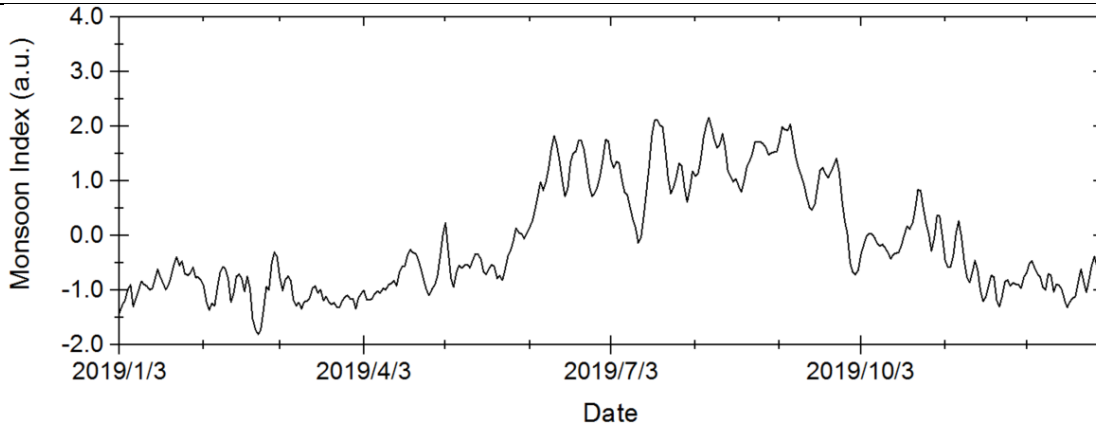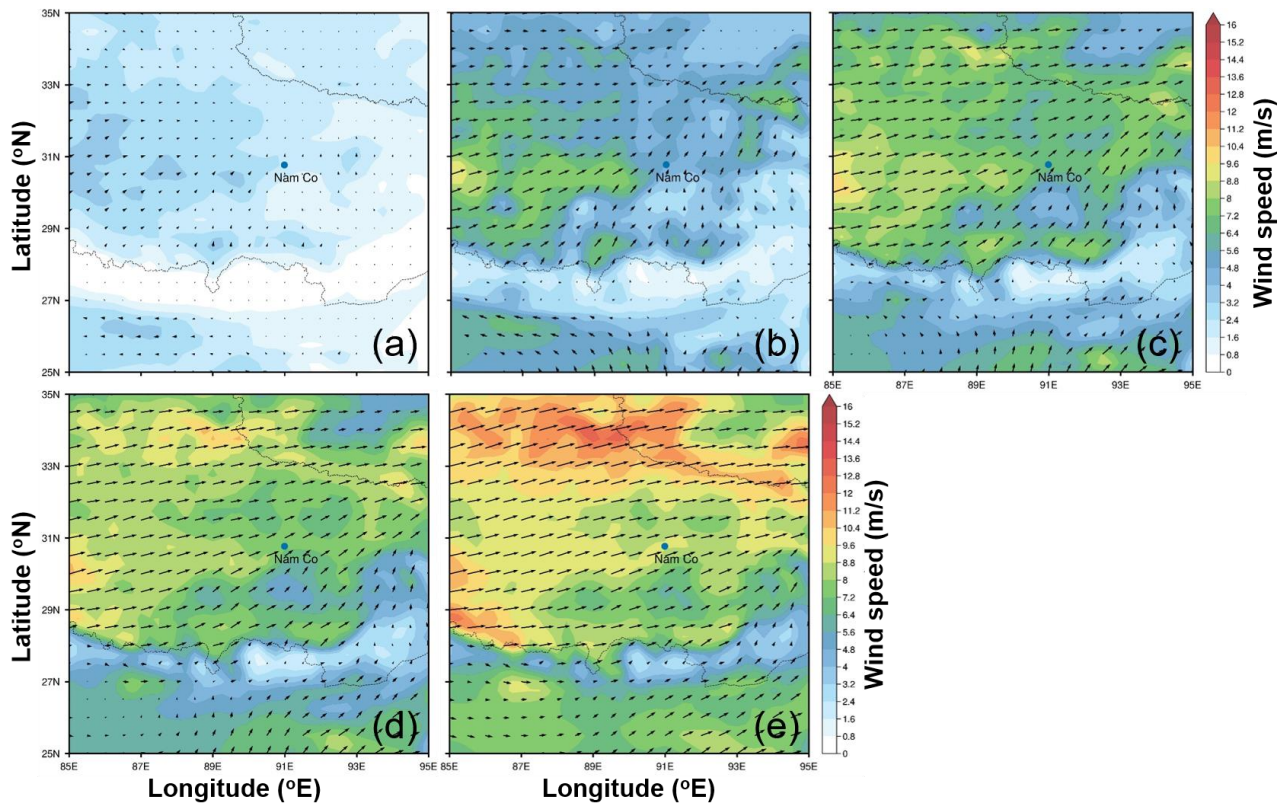
Figure S8. Ozone vertical profile measure by (a) TROPOMI at Nam Co, (b) lidar at Yangbajing (Feng et al., 2019), (c) ozonesonde at Qaidam (Zhang et al., 2020), and (d) lidar at Lhasa (Yu et al., 2022).
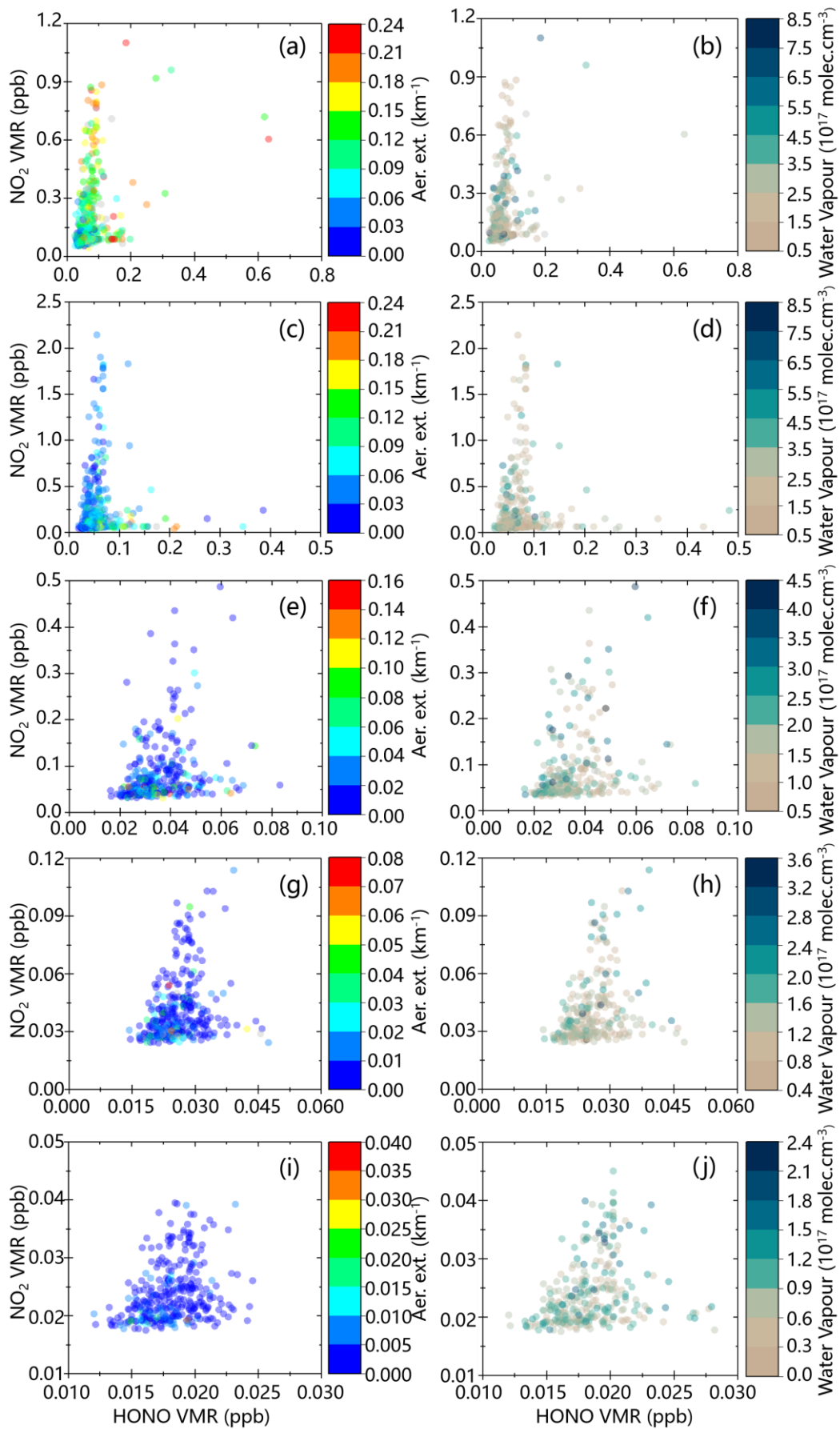
Figure S9. The Indian monsoon index during 2019.
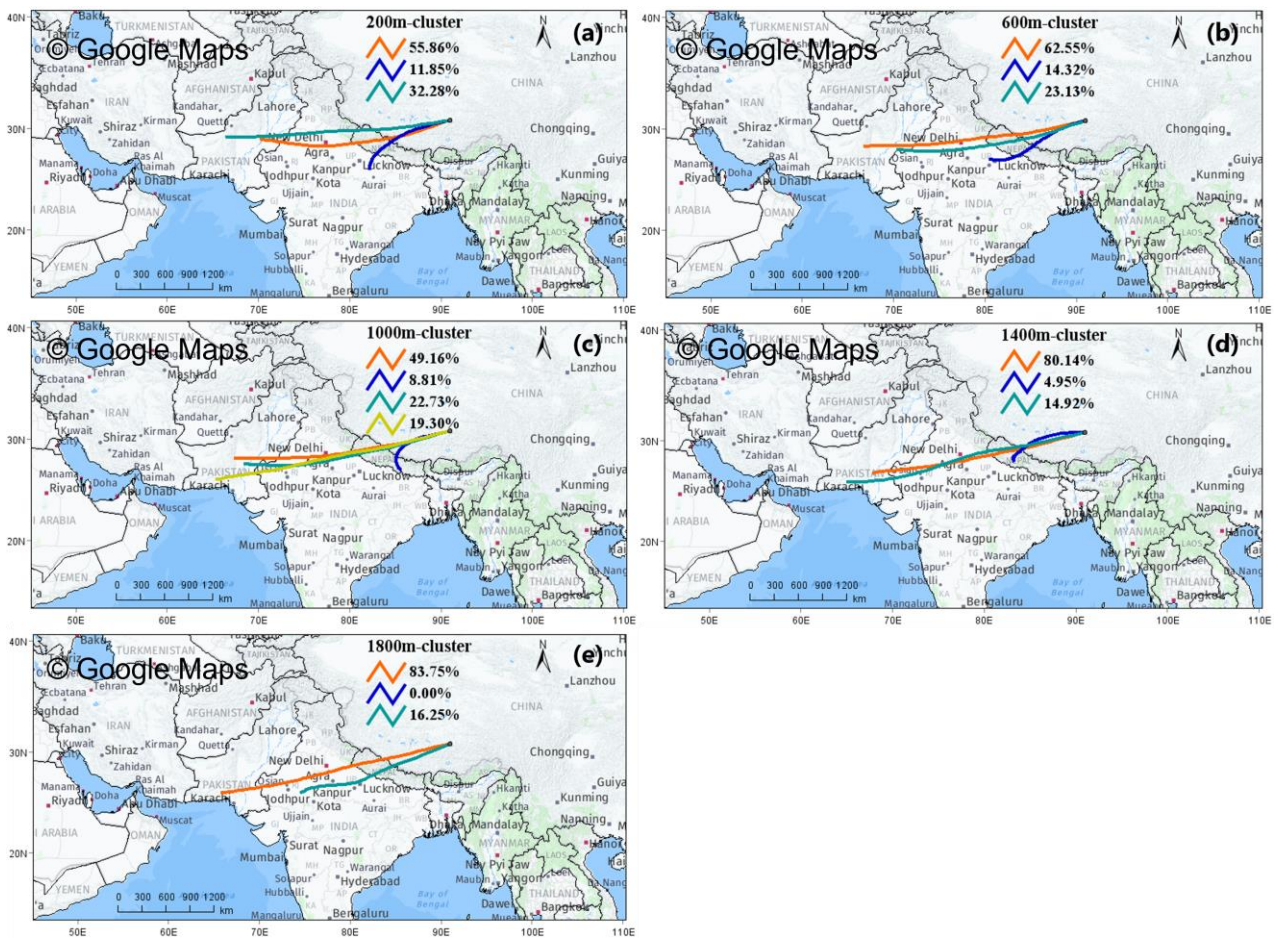
70

Figure S10. Wind direction and wind speed at (a) 10 m, (b) 500 m, (c) 1000 m, (d) 1300 m, and (e)
1800 m at a range of 25°N-35°N and 85°E-95°E, respectively.

Figure S11. Scatter plots of HONO vs NO$_2$ at (a-b) 0-0.2 km, (c-d) 0.4-0.6 km, (e-f) 0.8-1.0 km, (g-h) 1.2-1.4 km, and (i-j) 1.6-1.8 km coloured by aerosol extinction coefficients and water vapour in the top and bottom row, respectively, from 01 May to 09 July 2019.

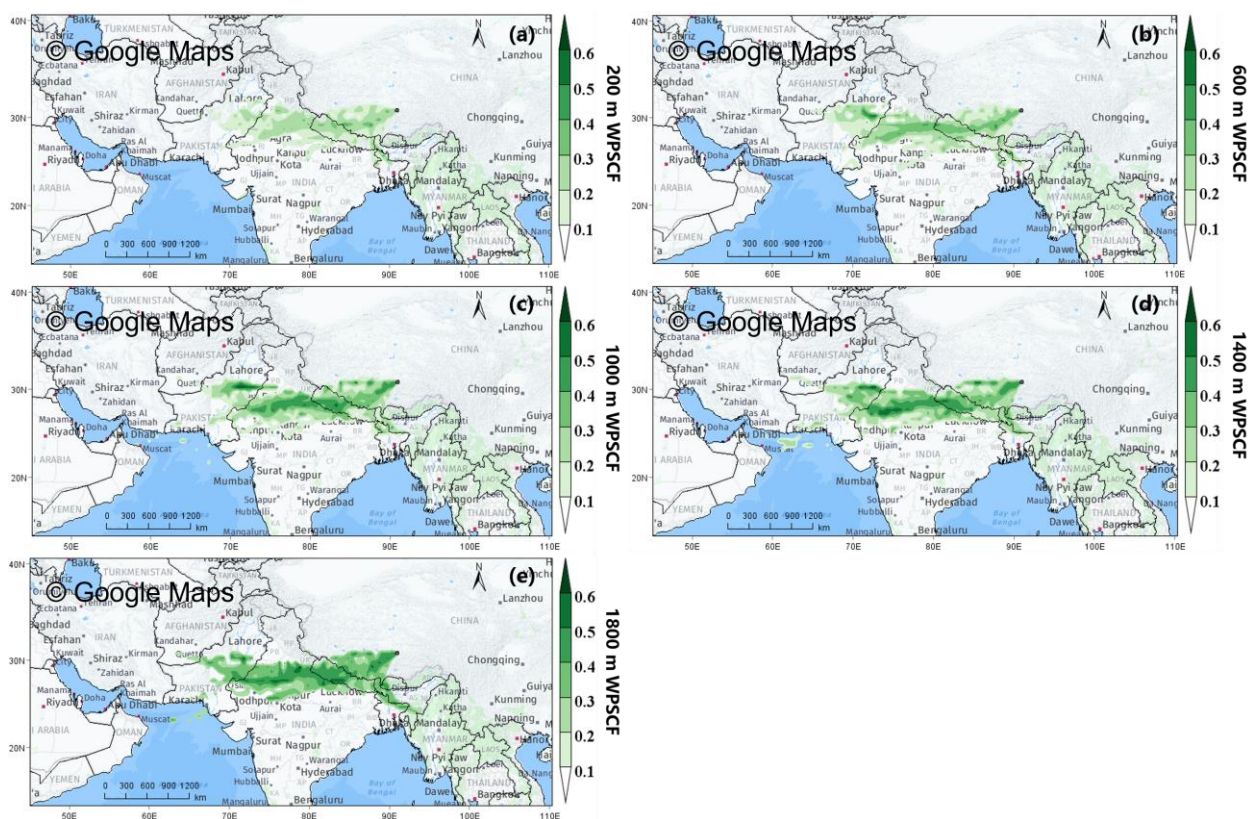79

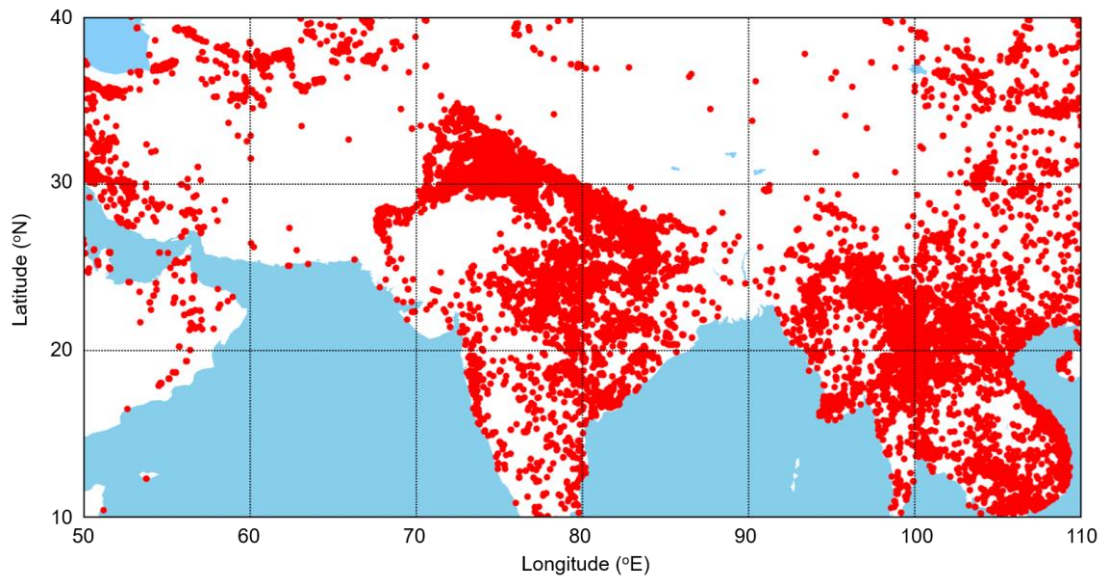Figure S12. The percentage of allocation to each mean 48-h backward trajectory cluster arriving at CAS (NAMORS) at (a) 200 m, (b) 600 m, (c) 1000 m, (d) 1400 m, and (e) 1800 m height layers from 01 May to 09 July 2019.

84
85 Figure S13. Spatial distributions of 48-h WPSCF values for O$_3$ at (a) 200 m, (b) 600 m, (c) 1000 m, (d)
86 1400 m, and (e) 1800 m height layers from 01 May to 09 July 2019 over CAS (NAMORS).
87

88
89 Figure S14. The spatial distribution of fire point in south Asian subcontinent from May to July 2019.
90
91

References

Fang, X., Li, T., Ban, C., Wu, Z., Li, J., Li, F., Cen, Y., and Tian, B.: A mobile differential absorption lidar for simultaneous observations of tropospheric and stratospheric ozone over Tibet, Opt. Express, 2019, 27(4), 4126-4139, doi:10.1364/OE.27.004126.

Yu, J., Meng, L., Chen, Y., Zhang, H., and Liu, J.: Ozone profiles, precursors, and vertical distribution in urban Lhasa, Tibetan Plateau, Remote Sens., 2022, 14(11), doi:10.3390/rs14112533.

Zhang, J., Xia, X., and Wu, X.: First in situ UV profile across the UTLS accompanied by ozone measurement over the Tibetan Plateau, J. Environ. Sci., 2020, 98, 71-76, doi:10.1016/j.jes.2020.05.020.

Iacono, M. J., Delamere, J. S., Mlawer, E. J., Shephard, M. W., Clough, S. A., Collins, W. D.: Radiative forcing by long-lived greenhouse gases: Calculations with the AER radiative transfer models, J. Geophys. Res., 2008, 113.

Grell, G. A., Freitas, A. R.: A scale and aerosol aware stochastic convective parameterization for weather and air quality modeling, Atmos. Chem. Phys., 2014, 13, 23845-23893.

Tewari, M., Chen, F., Wang, W., Dudhia, J., LeMone, M. A., Mitchell, K. M., Ek, G., Gayno, J., Wegiel, R., Cuenca, H.: Implementation and verification of the unified NOAH land surface model in the WRF model, Geoscience, 2004.

Hong, S. Y., Yign, N., Jimy, D.: A new vertical diffusion package with an explicit treatment of entrainment processes, Mon. Weather Rev., 2006, 134, 2318-2341.

Chen, S. H., Sun, W. Y.: A one-dimensional time dependent cloud model, J. Meteorol. Soc. Jpn., 2002, 80, 99-118.

Ji, X., Liu, C., Wang, Y., Hu, Q., Lin, H., Zhao, F., Xing, C., Tang, G., Zhang, J., Wagner, T.: Ozone profiles without blind area retrieved from MAX-DOAS measurements and comprehensive validation with multi-platform observations. Remote Sensing of Environment, 284, 113339, doi.org/10.1016/j.res.2022.113339, 2023.

Liu, C., Xing, C., Hu, Q., Li, Q., Liu, H., Hong, Q., Tan, W., Ji, X., Lin, H., Lu, C., Lin, J., Liu, H., Wei, S., Chen, J., Yang, K., Wang, S., Liu, T., Chen, Y.: Ground-based hyperspectral stereoscopic remote sensing network: A promising strategy to learn coordinated control of O_3 and $PM_{2.5}$ over China. Engineering, 19, 71-83, doi.org/10.1016/j.eng.2021.02.019, 2022.

Lin, H., Liu, C., Xing, C., Hu, Q., Hong, Q., Liu, H., Li, Q., Tan, W., Ji, X., Wang, Z., Liu, J.: Validation of water vapor vertical distributions retrieved from MAX-DOAS over Beijing, China. Remote Sensing, 12, 3193, doi.org/10.3390/rs12193193, 2020.

Xing, C., Xu, S., Song, Y., Liu, C., Liu, Y., Lu, K., Tan, W., Zhang, C., Hu, Q., Wang, S., Wu, H., Lin, H.: A new insight into the vertical differences in NO_2 heterogeneous reaction to produce HONO over inland and marginal seas. Atmospheric Chemistry and Physics, 23, 5815-5834, doi.org/10.5194/acp-23-5815-2023, 2023.